coatings

MDPI

Article

Individual Layer Thickness Dependence of Microstructure and Mechanical Properties of Magnetron Sputtering Mo-W-Doped Ni/Ni_3Al Multilayers

Chao Zhang [1,2,*], Lijun Shao [2], Yuming Dai [1], Duo Li [3] and Yuan Chen [4]

[1] School of Materials Science and Engineering, Nanjing Institute of Technology, Nanjing 211167, China
[2] Jiangsu Gongchang Roll Joint Stock Co., Ltd., Wuxi 214253, China
[3] China North Special Ammunition Research Institute, Qiqihar 161006, China
[4] Key Laboratory of Crop Harvesting Equipment Technology of Zhejiang Province, Jinhua Polytechnic, Jinhua 321017, China
* Correspondence: zhangchao@njit.edu.cn; Tel.: +86-25-86118274

Abstract: The mechanical properties of nanocrystalline pure Ni films are degraded due to grain coarsening with exposure for a long time in ambient. In order to further improve the mechanical properties of Ni-based thin films, as-sputtered Mo-W co-doped Ni/Ni_3Al multilayered structures were constructed. When the individual layer thickness (h) is lower than 40 nm, both the average grain sizes and the crystallinity degrees are degraded, showing a tendency for the formation of the amorphous phase. With h = 40 nm, nano-twins were observed as (111) twining interfaces for the multilayers due to the reduction of the stacking fault energy by the co-doping of Mo-W, whereas the nucleation and growth of the nano-twins were limited, without observations for the Mo-W co-doped Ni/Ni_3Al multilayer with h = 10 nm. The hardness of the multilayers was enhanced, and the elastic modulus was reduced at a lower h, owing to the grain refinements and layer interface barriers for strengthening, and the existence of the amorphous phase with the inferior modulus, respectively. The resistance against the fracture was enhanced due to toughening by the lamellar structure for the Mo-W doped Ni/Ni_3Al multilayer at h $\leq$ 40 nm. Comprehensively, the Mo-W-doped Ni/Ni_3Al multilayer with 10 nm displays a superior mechanical performance.

Keywords: Ni-based films; multilayers; sputtering; microstructure; mechanical properties

check for updates

Citation: Zhang, C.; Shao, L.; Dai, Y.; Li, D.; Chen, Y. Individual Layer Thickness Dependence of Microstructure and Mechanical Properties of Magnetron Sputtering Mo-W-Doped Ni/Ni_3Al Multilayers. *Coatings* **2022**, *12*, 1616. https://doi.org/10.3390/coatings12111616

Academic Editor: Claudia Barile

Received: 26 September 2022
Accepted: 20 October 2022
Published: 24 October 2022

Publisher's Note: MDPI stays neutral with regard to jurisdictional claims in published maps and institutional affiliations.

Copyright: © 2022 by the authors. Licensee MDPI, Basel, Switzerland. This article is an open access article distributed under the terms and conditions of the Creative Commons Attribution (CC BY) license (https://creativecommons.org/licenses/by/4.0/).

1. Introduction

Recently, the structural components in microelectromechanical systems (MEMS) should meet the requirements of maintaining good thermal conductivity, oxidation resistance, and mechanical properties [1,2]. Based on the above service requirements, nanocrystalline Ni thin films have been widely used in structural components, such as micro-springs, gears, and cantilevers in MEMS because of their excellent mechanical performance and formability [3,4]. However, the hardness of pure Ni films decreases significantly due to the rapid grain growth above 300 °C [5] and even the self-annealing of fine-grained, nonequilibrium microstructure of pure nanocrystalline Ni film leads to grain coarsening and a drop in the mechanical properties with exposure for a long time in ambient [6,7]. The addition of elements such as Co [8], Mn [9], Mo [10], and W [11] to form binary Ni alloys are suitable approaches to confine grain coarsening and further improve the mechanical properties of nanocrystalline Ni-based films. Among them, the alloying of pure Ni films by the W element can inhibit grain growth with an improvement of strength, significantly. The relevant reports found that binary Ni-W films prepared by electroplating show grain refinements with good hardness [11,12]. However, it is difficult to accurately control the composition and microstructure of Ni-W films by electroplating, and wastewater with heavy metal ions is produced in the preparation process, which is not in accordance with the

development trend of green manufacturing [13]. Compared with the preparation of Ni-W films by electroplating, magnetron sputtering can accurately modulate the composition and microstructure of Ni-W films, so as to obtain Ni-based films with excellent properties [14]. Borgia et al. sputtered Ni-75 at.% W film with hardness reaching 17 GPa [15]. However, higher internal stress in the Ni-W film will promote the formation of micropores in the Ni-W film [16,17]. By studying the fracture toughness of Ni-W films, Armstrong [18] and Yin [19] found that the aggregation of micropores in the films eventually led to the fracture failure of the films. Therefore, the addition of an excessive W content ($\geq$20 at.%) will adversely affect the properties of Ni-based films.

To overcome these shortcomings of Ni-W thin films, the recent sputtering of Ni-Mo-W ternary films with no more than 6 at.% W additions, showing an extraordinary balance of strength and toughness, underpinned by the formation of the growth of nano-twins [20,21]. Due to this suite of properties, Ni-Mo-W films possess a lower and tailorable coefficient of thermal expansion [22] and are compatible with the wafer-level manufacturability of metal MEMS devices [23]. In addition, recent research focuses on the use of the ternary formulation of the Ni-Mo-W catalyst with improved hydrogenation functions [24,25]. This is due to the well-known hydrogenation properties of Ni and the higher hydrogenation capacity of W with respect to Mo [26], which are also used as cathodes for hydrogen production using electrolysis from water [27]. However, Mo atoms exhibit weaker inhibition on grain growth compared with W atoms; the enhancement of the microstructure stability and hardness for Mo-W-doped Ni-based film is limited [21]. To further improve the mechanical properties of as-sputtered nanocrystalline thin films, the combination of the elements doped, and the nanoscale multilayer architecture can provide the strategy to achieve [28–34]. The advantages of synergistic layer interfaces and elements solution strengthening can be expected for novelty element-doped multilayers, such as MoS_2-based [28,29], transition metal nitride-based [30–32], carbon-based [33], and Ni-based multilayers [34], where the layer interfaces act as barriers to the grain boundaries and dislocations' movement. In our previous studies, W-doped Ni/Ni_3Al multilayers with an individual layer thickness of 40 nm showed significate hardness and wear resistance under the synergistic strengthening effect of the W alloying and multilayered structure [34,35]. Many reports reveal that the effects of the phase and interface microstructure are adjusted by the individual layer thicknesses on the strengthening of multilayer films composed of modulation layers [31,36,37]. However, the influence of the individual layer thicknesses on the microstructure and mechanical properties of as-sputtered Mo-W-doped Ni-based multilayer coatings is still unclear and is expected to be further improved.

In order to further improve the mechanical properties of Ni-based thin films, as-sputtered Mo-W co-doped Ni/Ni_3Al multilayers were constructed with 5 at.% Mo and 5 at.% W co-additions and the individual layer thicknesses at 10~160 nm. The individual layer thickness, dependent on the microstructure and mechanical properties of the as-sputtered Mo-W co-doped Ni/Ni_3Al multilayer, was investigated and expounded. Consequently, the strengthening mechanism of the as-sputtered Ni-based films induced by Mo-W multi-elements dopants and nano-multilayer architecture were also revealed.

2. Materials and Methods

Mo-W doped Ni/Ni_3Al multilayered films (hereafter referred to as the *h* Ni/Ni_3Al-MoW multilayer, where *h* is the individual layer thickness) were deposited on a Si (100) (99.99% in purity) wafer by direct-current (DC) magnetron sputtering using an MPB-300B coating system (Beijing Chuangshiweina Technology, Beijing, China). The substrate was ultrasonically cleaned and dried. Before deposition, the vacuum chamber was evacuated to a base pressure of 8.0×10^{-4} Pa. Sputter etching with a bias voltage of -300 V was employed in an Ar environment for 30 min to remove surface contaminants from the substrate. Deposition of the Ni/Ni_3Al-MoW multilayers was conducted at a pressure of 2 Pa (75 sccm Ar (99.9% in purity) flow rate) using a pure Ni target (100 at.% Ni), Ni-25 at.% Al (74.9 at.% Ni, 25.1 at.% Al, hereafter referred to as Ni_3Al) alloy target, and

Mo-50 at.% W (50.0 at.% Mo, 50.0 at.% W, hereafter referred to as MoW) alloy target with a purity of 99.9%. The modulated Ni-MoW and Ni_3Al-MoW layers were deposited through co-sputtered Ni (fixed power at 100 W), Ni_3Al (fixed power at 80 W), and MoW targets. Simultaneously, the modulated layered structure with different h was prepared via alternation of the sputtering/closing time of Ni and Ni_3Al targets, according to the deposition rates. During deposition, the first layer on the substrate was a Ni-MoW layer and the top layer was the Ni_3Al-MoW on the surface, and the total film thickness was about 900 nm. The important processing parameters and chemical composition of the films are listed in Table 1.

Table 1. Typical magnetron sputtering, structure, and composition parameters of multilayers.

Samples	Sputtering Time (s)	Individual Layer Thickness (nm)	Element Compositions of Monolayer Films (at.%)
10 nm Ni/Ni_3Al-MoW	Ni-MoW 33 (45) Ni_3Al-MoW 32 (45)	Ni-MoW 10 (45) Ni_3Al-MoW 10 (45)	Ni 89.6; Mo 5.1; W 5.3 Ni 66.7; Al 23.8; Mo 4.9; W 4.6
40 nm Ni/Ni_3Al-MoW	Ni-MoW 130 (12) Ni_3Al-MoW 128 (12)	Ni-MoW 40 (12) Ni_3Al-MoW 40 (12)	Ni 90.1; Mo 5.1; W 4.8 Ni 73.3; Al21.1; Mo 5.2; W 5.4
160 nm Ni/Ni_3Al-MoW	Ni-MoW 520 (3) Ni_3Al-MoW 515 (3)	Ni-MoW 160 (3) Ni_3Al-MoW 160 (3)	Ni 88.9; Mo 5.5; W 5.6 Ni 72.7; Al 16.5; Mo 5.3; W 5.5

( ) represents the number of individual layers for Ni/Ni_3Al-MoW multilayers.

The microstructure of the Ni/Ni_3Al-MoW multilayers was investigated by X-ray diffraction (XRD) and transmission electron microscopy (TEM). XRD was performed on a Rigaku D/max 2500 diffractometer (Rigaku Ltd., Tokyo, Japan) with Cu Kα radiation (λ = 0.15406) at room temperature with an angle range of 2θ = 30~68°. According to Debye–Scherrer's equation [38], the XRD results can be used to calculate the average grain size d_{XRD} of nanocrystalline films:

$$d_{XRD} = K\lambda/\beta \cos\theta \quad (1)$$

where K is Debye–Scherrer's constant, generally K = 0.9, λ is the X-ray wavelength (λ = 1.5406 nm), β is the width at half maximum (FWHM) of the sample after deducting the diffraction width of the instrument itself is expressed in the radian unit, rad, and θ is the Bragg diffraction angle. The grain size calculated by Debye–Scherrer's equation is close to the actual size, which is in the range of 1~100 nm. The on-top surface and cross-sectional microstructures of the Ni/Ni_3Al-MoW multilayers were observed by a field emission scanning electron microscope (FESEM, Zeiss Merlin Compact, Jena, Germany). The three-dimensional surface topographies were performed by an atomic force microscope (AFM) using a Nanonavi E-Sweep instrument (SII NanoTechnology Inc., Tokyo, Japan) and the RMS (root-mean-square) surface roughness was calculated by Nanonavi E-Sweep software extracted from the three-dimensional surface topographies automatically. The cross-sectional TEM (XTEM, Tecnai G^2 F20 S-TWIN, FEI Company, Hillsboro, CA, USA) samples were prepared by mechanical grinding and polishing followed by thinning to an electron transparent thickness by low-energy (3.5 keV) Ar ion milling and subsequent ion polishing (Gatan PIPs, model 691, Berwyn, PA, USA). The modulation and interface of the cross-sectional multilayers were observed by the TEM at 200 kV.

In order to reflect the mechanical properties varying the microstructures of the Ni/Ni_3Al-MoW multilayers, the hardness was determined on an Agilent Nano Indenter G200 nanoindention tester (Agilent Technologies, Santa Clara, CA, USA) equipped with a Berkovich indenter standard Berkovich tip at room temperature. To eliminate the effects of the hard substrate, the peak load was 1.5 mN by employing the load-controlled mode, and the penetration depth was no more than 10% of the total coating thickness. Ten indents were performed on every sample. Each test was set at a loading rate of 0.1 mN/s and an unloading rate of 0.05 mN/s. The holding time of 20 s at the maximum load was selected to saturate the creep effects before unloading. The hardness of the multilayered films for

each load was derived from the load depth indentation curves using the Oliver and Pharr method [39], assuming a Poisson ratio of 0.3.

3. Results and Discussion

3.1. The Microstructure

Figure 1 shows the top-surface morphologies of the as-sputtered Ni/Ni_3Al-MoW multilayers under the scanning electron microscope (SEM). As shown in Figure 1, the particles as typical island structures are observed on the surface of the Ni/Ni_3Al-MoW multilayers with varying h due to the agglomeration of deposited atoms during sputtering. There are also no defects, such as holes and cracks, on the top-surface morphology of the multilayer. It can be found that the size and globular shape of the particles on the surface of the multilayered films with h = 160 nm and 40 nm are relatively uniform. However, when h = 10 nm, the average size of the globular particles is decreased slightly, and there are some larger particles among the finer particle island structures, showing the abnormal growth of the particles on the top-surface. This can be attributed to the growth rates of the particles in the island structure, which are determined by the deposition rates, which are more variable with the increments of the frequency of the alternate sputtering of the Ni target and Ni_3Al target for the multilayer with h = 10 nm. This leads that the globular particles' size exhibits a discrepancy at varying growth rates, and the existence of a few coarsened particles is demonstrated.

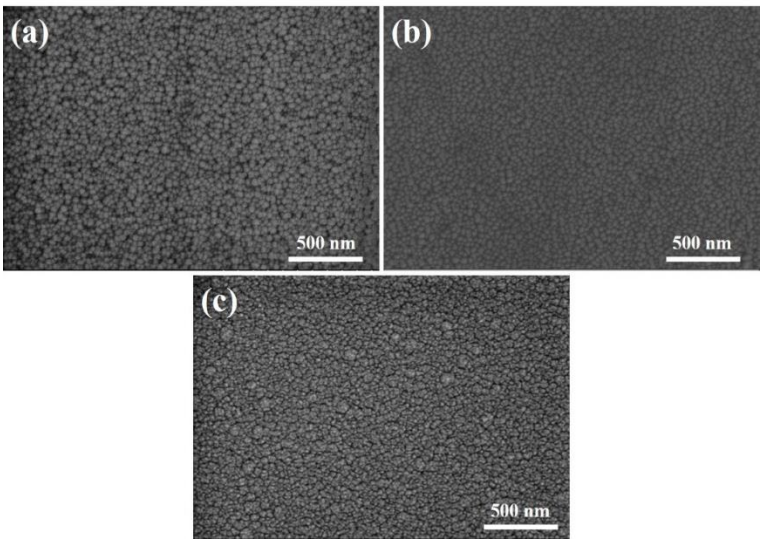

Figure 1. Top-surface SEM images of Ni/Ni_3Al-MoW multilayer with varying h: (**a**) 160 nm; (**b**) 40 nm; (**c**) 10 nm.

During the magnetron sputtering process, the growth of the Ni/Ni_3Al-MoW multilayers was formed by the condensation of a large number of Ni, Al, Mo, and W atoms and corresponding atomic clusters on the surface of the substrate. When the multilayers were sputtered at ambient, without heating the substrate, cone-shaped nano-particles were distributed on the surface without continuous, long trenches or blotches, as shown in Figure 2. It is worth noting that some of the particles are irregularly stacked, forming bright and dark regions with height fluctuation of the particles, which does not exceed 25 nm for the Mo-W doped Ni/Ni_3Al multilayers. It indicates that the significant roughness of the surface is presented and varied with the h for the multilayers. The RMS (root-mean-square) surface roughness was calculated by the formulation, as follows [40]:

$$\mathrm{RMS} = \left[\frac{1}{N}\sum_{i=1}^{N}(Z-\bar{Z})^2\right]^{\frac{1}{2}} \quad (2)$$

where N is the number of the surface height, Z represents the maximum height, and $\bar{Z}$ is the average height of the examined area, respectively. As shown in Figure 2, the roughness of the as-sputtered multilayer ranges from 2 nm to 4 nm. With h $\leq$ 40 nm, the surface roughness decreases due to the lower height fluctuation of the particles within the surface, resulting from the refinement of the nano-particles by the layer interfaces, without obvious aggregation and excessive stacking, both in the plane and vertical directions. For the Ni/Ni_3Al-MoW multilayered film with h = 10 nm, the particles on the surface of the multilayer exhibit obvious fluctuations in their height due to the variation of the growth rates for the particles induced by frequent alternative sputtering Ni-MoW and Ni_3Al-MoW layers, and thus the surface roughness is increased slightly. The improved surface quality with inferior roughness is provided by the modulation of a periodical h for the Mo-W doped Ni/Ni_3Al multilayered films.

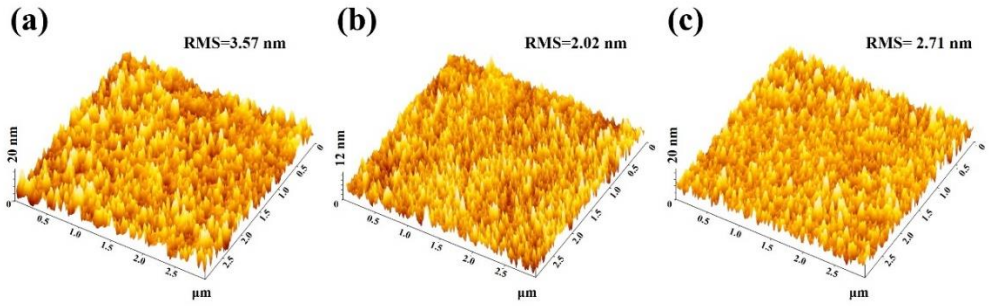

Figure 2. AFM three-dimensional morphology and calculated RMS results of Ni/Ni_3Al-MoW multilayers with different *h*: (**a**) 160 nm; (**b**) 40 nm; (**c**) 10 nm.

Figure 3a shows that the diffraction peaks of the γ-Ni-based solid solution phase with a face-centered cubic (FCC) structure coincide on the (111) and (200) crystal planes for the Ni/Ni_3Al-MoW multilayers with h = 160 nm and 40 nm. This indicates that the lattice difference of the γ-Ni-based solid solution phases between the Ni-MoW and Ni_3Al-MoW layers is very small. Under the effect of the compressive internal stress of the as-sputtered multilayer, the solid solution of the Mo-W elements causes a slight lattice distortion, leading to the lattice constants between the Ni-MoW and Ni_3Al-MoW layers being almost the same, without an obvious lattice mismatch. Compared with the intensities of the diffraction peaks, it is found that the diffraction peak on the (111) plane is the strongest, which indicates that the deposited thin film exhibits the (111) plane texture. The multilayers grow along the (111) direction due to the minimum surface energy of the (111) plane for the FCC-structured γ-Ni-based solid solution, and thus the deposited atoms tend to stack on the close-packed (111) plane in order to reduce the surface energy. In this paper, no form of external heat source was applied to the substrate during the sputtering process. Once the atoms were deposited on the surface of the film, it was difficult to rearrange them by diffusion. Therefore, the as-sputtered multilayer shows a strong texture on the (111) plane. The average crystalline or grain size calculated by Debye–Scherrer's equation inside the multilayers, as shown in Figure 3b, decreases with the reduction of h for the increment of the peak width at half the height (FWHM) of the γ-Ni (111) diffraction peak, indicating that the layer interfaced within the multilayers can inhibit the grain growth. When h = 10 nm, it is worthy to note that attenuated and broad in γ-Ni (111) peaks can be detected at 2θ between 42° and 46°, showing a lower crystallinity. This implies that the formation of the amorphous phase is promoted [41], resulting from disordered atom arrangements induced by more interfaces with a lower h.

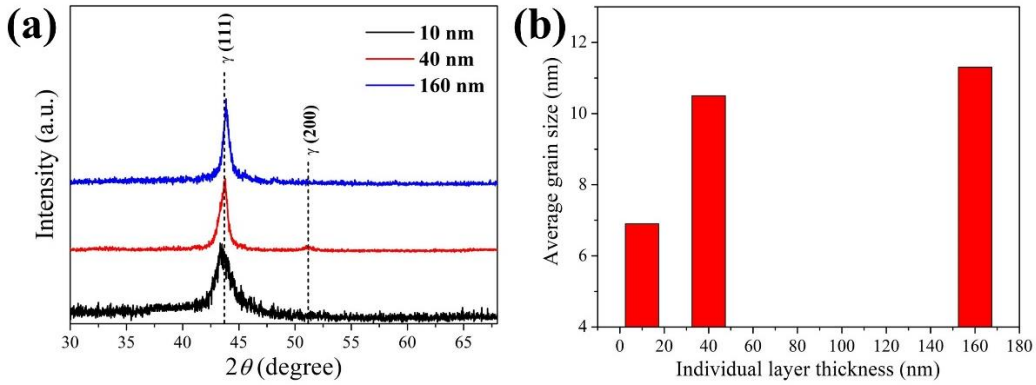

Figure 3. (**a**) XRD results of Ni/Ni_3Al-MoW multilayers and (**b**) average grain sizes calculated by Debye–Scherrer's equation with h = 10 nm, 40 nm, and 160 nm.

The cross-sectional FE-SEM images at a high magnification of the as-sputtered Ni/Ni_3Al-MoW multilayers are shown in Figure 4. It can be seen that the sharp interfaces are presented between alternating layers within the sputtered Ni/Ni_3Al-MoW multilayers for h = 160 nm and 40 nm, and the h is consistent with the designed value of the multilayers. When h = 10 nm, the layer interfaces in the lamellar structure are obscured due to the limitation of the SEM resolution for the observations, presenting a cross-sectional morphology similar to that of the monolayer film. In addition, the columnar crystal structures are observed, as shown in the cross-sectional morphology of the as-sputtered multilayers. Combined with the AFM and XRD characterization results, the Ni/Ni_3Al-MoW multilayered film grows as columnar crystals along the normal direction of the (111) plane. According to the Structure Zone Model [42,43], when $T_{dep}/T_m < 0.458$, the grains of the films grow as columnar structures and the direction is perpendicular to the film/substrate interface, where T_{dep} is the deposition temperature ($\leq$100 °C), and T_m is the melting point of the Ni-5 at.% Mo-5 at.% W alloy (about 1450 °C) [44]. Thus, the columnar grains are observed for all the Ni/Ni_3Al-MoW deposited at room temperature due to the condition agreement of the abovementioned Structure Zone Model.

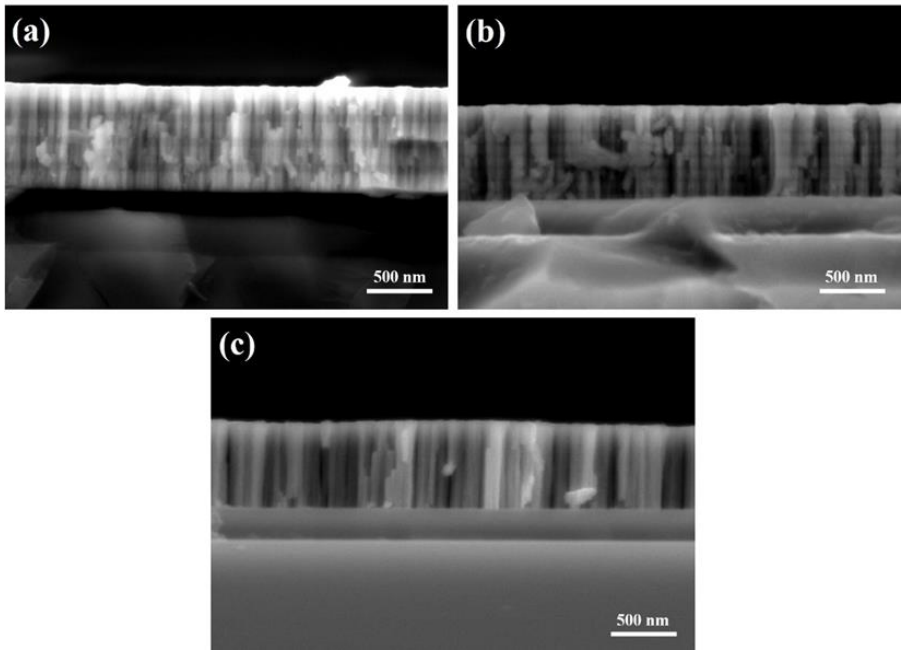

Figure 4. Cross-sectional FE-SEM images of as-sputtered Ni/Ni_3Al-MoW multilayers with different *h*: (**a**) 160 nm; (**b**) 40 nm; (**c**) 10 nm.

In order to characterize the finer microstructure of the films clearly, the cross-sectional BF-TEM observation of the representative h = 10 nm and 40 nm Ni/Ni_3Al-MoW multilayers was utilized, as shown in Figure 5a,b, respectively. It can be found that the contrast between the Ni-MoW and Ni_3Al-MoW layers is different, showing a typical lamellar structure with sharp and straight layer interfaces in Figure 5a. The layered structure with a brighter contrast is the Ni_3Al-MoW layers; on the contrary, the layers with the darker contrast are the Ni-MoW layers, due to more difficulty of the transmitted electron beam to pass through the phases of the Ni-MoW layers. As demonstrated in the inset of Figure 5a, the corresponding SAD results indicate that the diffraction rings of the Ni-MoW layers and Ni_3Al-MoW layers in the multilayers with h = 40 nm overlap each other, showing the FCC-structured γ-Ni-based solid solution phases. The γ-Ni (111) diffraction ring exhibits a brighter contrast, further confirming that the texture plane of the multilayer is (111). Figure 5b shows that the volume proportions of the layer interfaces increase significantly for the multilayered film with h = 10 nm, presenting the lamellar structure. A careful observation of the SAD results corresponding to the multilayered film, as illustrated in the inset of Figure 5b, shows that both a broad halo and bright γ-Ni (111) diffraction ring are observed, verifying the coexistence of amorphous and nanocrystalline structures of the Ni/Ni_3Al-MoW, multilayered with the induction of more layer interfaces at a smaller h.

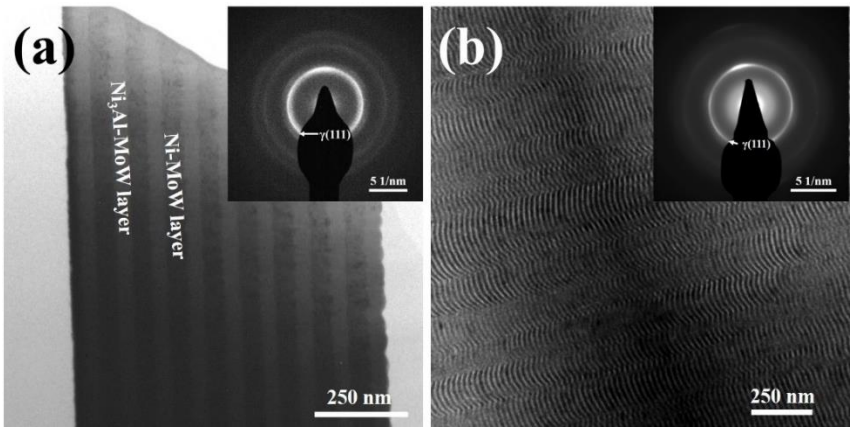

Figure 5. The representative cross-sectional bright fields (BF) TEM image: (**a**) *h* = 40 nm; (**b**) *h* = 10 nm, and corresponding selected area electron diffraction results of Ni/Ni_3Al-MoW multilayers are shown in the inset.

Figure 6a shows that the twins are displayed in a region between the space of the two adjacent layer interfaces of the 40 nm Ni/Ni_3Al-MoW multilayer. By the fast Fourier transformation of the squared region marked A near the nano-twins in Figure 6a, it can be found that the lattice fringes are interpreted as the γ-Ni-based solid solution phase, and the twin planes are mainly γ (111) with an angle between them of 118°. The formation of the twins within the 40 nm Ni/Ni_3Al-MoW multilayer can be attributed to the reduction of the stacking fault energy (SFE). Among the many kinds of common additive elements in Ni-based alloys, Mo and W are two of the most effective alloying elements to reduce the SFE in Ni [45]. Thus, the SFE is significantly reduced, and it promoted the formation of nano-twins with the co-alloying of the Mo and W elements in the Ni/Ni_3Al multilayer with h = 40 nm. Meanwhile, the sputtering Ni/Ni_3Al multilayers with the Mo-W dopant can also improve the deposition rates of the films, leading to further facilitating the formation of nano-twins. When h =10 nm, the arrangement of lattice fringes in the Ni/Ni_3Al multilayers is relatively disordered, as demonstrated in Figure 6b, showing a strong tendency for amorphization. The γ-Ni-based solid solution phase is also verified by the fast Fourier transform result of the square B region with a crystalline domain. The lack of twins is observed in the HRTEM of the 10 nm Ni/Ni_3Al-MoW multilayer. It is reported that the alleviated coherency stress can determine the formation of twins [46,47]. In order to generate the nuclei of the twin

interface, a leading partial dislocation must be emitted within the region of the grain boundary, which has high-density dislocations. Then, a twinning partial dislocation of the same Burgers vector on the adjacent slip plane is released. Subsequently, a series of atoms near the nucleation are stacked continuously along the direction of the two partial dislocations to increase the size of the twins. A critical h_p for the multilayered film is required for the basic stacking size of nucleation and growth during the nano-twins formation. In this case, when the coherent elastic strain energy, caused by the coherent mismatch, is equal to the tension of the leading dislocation line, the critical h_p for the nano-twin nucleation and growth in the Ni/Ni_3Al-MoW multilayer can be calculated according to the following [48]:

$$\frac{1}{2}\mathbf{b}^2 = fh_p\mathbf{b}_p \cos\lambda \cdot \frac{2(1+v)}{1-v} \quad (3)$$

where **b** is the Burgers vector of the dislocation with the value of 0.255 nm, according to the XRD results, and the average Poisson's ratio υ is 0.33 for the Ni-based-films, and λ is the angle between the slip plane and the layer interface. For the Ni/Ni_3Al-MoW multilayers, both the layer interface and the slip plane are (111) planes, so the angle of λ between them is 0. $\mathbf{b}_p$ is the Burgers vector of the partial dislocation with its numerical value of $\mathbf{b}/\sqrt{3}$, which is equal to 0.146 nm. f is less than 0.5% as the mismatch degree between the Ni-MoW layers and Ni_3Al-MoW layers within the 10 nm Ni/Ni_3Al-MoW multilayers, according to the XRD results in Figure 3a and the HRTEM results in Figure 6b. The critical calculated h_p is 13 nm for considering the multilayered structure. Therefore, when h is greater than 13 nm, sufficient space between the layer interfaces for the atomic stacking of the twin nucleation is provided within each layer in the Ni/Ni_3Al-MoW multilayers. Whereas the actual h in the 10 nm Ni/Ni_3Al-MoW multilayer is less than the critical h of 13 nm, the basic stacking size is not required for nucleation and growth in the process of twin formation. Thus, the nano-twins formation is not observed in the Ni/Ni_3Al-MoW multilayer with h = 10 nm.

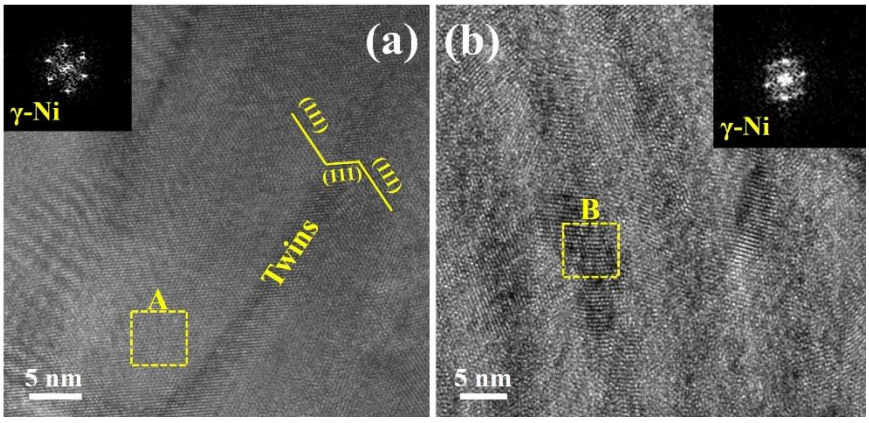

Figure 6. The HRTEM images of Ni/Ni_3Al-MoW multilayers with varying *h*: (**a**) *h* = 40 nm and (**b**) *h* = 10 nm, and corresponding fast Fourier transformation results of squared regions marked A and B are shown in the inset of (**a**,**b**) respectively.

3.2. Mechanical Properties

The hardness (*H*) measured by the nano-indentation of the Ni/Ni_3Al-MoW multilayers are shown in Figure 7a, and the hardness increments of the multilayers with a decrease of h are founded. The hardness of the 10 nm Ni/Ni_3Al multilayer exhibits an optimal value of 9.1 ± 0.4 GPa, which is slightly higher than the NiW/NiWAl multilayer with h = 40 nm in our previous study [35]. Note that the hardness of the multilayer increases significantly due to an obvious strengthening effect of the lamellar structure, whereas the strengthening effect of the layered structure with more layer interfaces is limited for the

Ni/Ni_3Al-MoW multilayers with lower than 40 nm. Each layer in the Ni/Ni_3Al-MoW multilayers mainly consists of the γ-Ni-based solid solution phase, with a little discrepancy in the lattice constant, and thus the shear modulus difference between the Ni-MoW and Ni_3Al-MoW layers is quite small, without the formation of Koehler stress for strengthening [49]. In addition, there is no hole and cracks without a peeling phenomenon for the as-sputtered multilayers. Consequently, co-deformation is provided between the Ni-MoW and Ni_3Al-MoW layers in the multilayered film during the loading of stress, rendering that the hardness value of the as-sputtered Ni/Ni_3Al-MoW multilayer can be predicted by the rule of mixing (ROM) in this case [50,51]. On the other hand, due to the Mo and W dopants, the grain sizes in the films are refined effectively with h $\leq$ 40 nm. As the dislocations pile-up around the grain boundaries and layer interfaces, the strengthening effect of the grain boundary on the hardness increment of the nanocrystalline Ni/Ni_3Al-MoW multilayers should be considered. Therefore, in terms of the grain refinement of the film combined with the Hall–Petch relationship in the as-sputtered Ni/Ni_3Al-MoW-multilayered film, a modified ROM of the hardness for the Ni-W and Ni_3Al-MoW layers is obtained as the following:

$$H_{\mathrm{ROM}}^{\mathrm{mod}} = V_{\text{Ni-MoW}}(H_0^{\text{Ni-MoW}} + k_{\text{Ni-MoW}} d_{\text{Ni-MoW}}^{-1/2}) + V_{\text{Ni}_3\text{Al-MoW}}(H_0^{\text{Ni}_3\text{Al-MoW}} + k_{\text{Ni}_3\text{Al-MoW}} d_{\text{Ni}_3\text{Al-MoW}}^{-1/2}) \quad (4)$$

where H_0 is the intrinsic strength of the coarse-grained sample, k is the Hall–Petch slope, and d is the equivalent grain size of the films with layer interfaces. V is the volume fraction with $V_{\text{Ni-MoW}} = V_{\text{Ni}_3\text{Al-MoW}} = 0.5$, and H_{ROM} is the hardness of the multilayer. According to the previous experimental results, the d decreases with a lower h. The hardness with a value of about 7~8 GPa [52] and 7.8 GPa [53] was used for the as-deposited monolithic Ni-W film and Ni_3Al-W film at a content of 4.5 at.%, respectively, which shows similar equivalent grain sizes to the Ni/Ni_3Al-MoW multilayers with both h = 160 nm and 40 nm. Likewise, the hardness of the Ni-W film and Ni_3Al-W film was at a content of 12.5 at.% is 8~9 GPa [52] and 8.5 GPa [53], respectively, due to their similar grain sizes with the 10 nm Ni/Ni_3Al-MoW multilayers. The hardness estimated by the modified ROM of the hardness with the Hall–Petch relationship matches reasonably well with the experimental value for the Ni/Ni_3Al-MoW multilayer with h = 160 nm. The maximum hardness of the Ni/Ni_3Al-MoW multilayer presents higher than the modified ROM of the hardness estimations, suggesting that the interface strengthening mechanism described [54–56] as an effect of the confined layer slip (CLS) of single-dislocation loops within the confined geometry and interface strength barrier underpinnings of the layer interface for h = 40 nm and 10 nm, respectively. The low crystallinity with an amorphous constitution is present in the Ni-MoW and Ni_3Al-MoW layers, leading to hardly emitted dislocations from the GBs with pinning, pre-existing dislocations. The existence of the nano-twin is also benefit to retard the dislocation slip [45], leading to a slight enhancement of the hardness for the 40 nm Ni/Ni_3Al-MoW multilayer. Therefore, the strengthening mechanism of the Ni/Ni_3Al-MoW multilayers is mainly caused by grain refinement and the existence of layer interfaces.

Figure 7b shows the curve of the elastic modulus (E) measured by the nano-indentation of the Ni/Ni_3Al-MoW multilayers. Compared with the γ-Ni-based solid solution, the elastic modulus of the amorphous phase is quite inferior [57,58]. Consequently, it can be found that the elastic modulus of the Ni/Ni_3Al-MoW multilayer decreases with a lower h as the reduction of crystallinity with more amorphous phase existence. This case is similar to the NiW/NiWAl multilayer in our previous study [35], which showed a smaller value of 151.1 ± 3.4 GPa in the elastic modulus. To be noted is the H/E ratio, which is also called the elastic strain to break and is related to the fracture toughness of the coating materials [59]; the ratio value of both the Ni/Ni_3Al-MoW multilayers with h = 10 nm (0.054) and h = 40 nm (0.050) is superior to that of the 160 nm Ni/Ni_3Al-MoW multilayer (0.042). This infers that the higher resistance against the fracture for the 10 nm Ni/Ni_3Al-MoW multilayer is due to the enhancement of its toughness with a deflection of the micro-crack by the increment of layer interfaces [60].

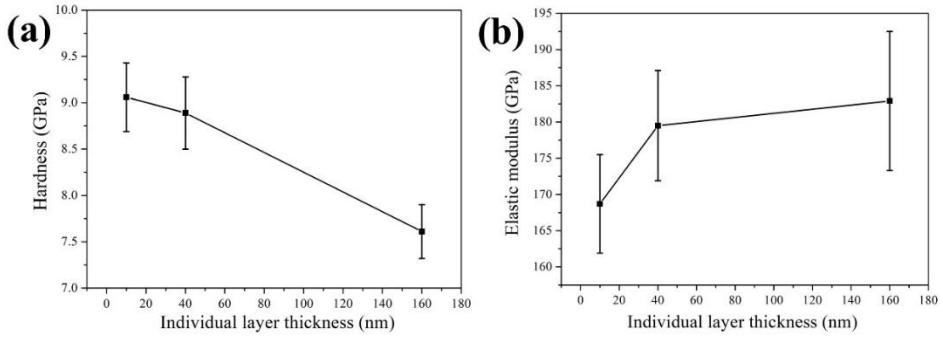

Figure 7. (**a**) The hardness and (**b**) the elastic modulus measured by nano-indentation of Ni/Ni_3Al-MoW multilayers plotted as a function of *h*.

4. Conclusions

The Ni/Ni_3Al-MoW multilayer with h = 10 nm, 40 nm, and 160 nm were prepared by DC magnetron sputtering, and their microstructures and mechanical properties were investigated. Based on the obtained results, the following conclusions can be drawn:

(1) All of the Ni/Ni_3Al-MoW multilayers exhibited finer globular particles and lower roughness without micro-cracks and holes in the surface morphologies. The phase composition of the multilayer was identified as a γ-Ni-based solid solution phase dominantly, presenting the (111) texture;

(2) With a lower *h*, the average grain size of the Ni/Ni_3Al-MoW multilayers decreased, and the crystallinity degrees were degraded with the existence of the amorphous phase structure at a slight amount. In addition, nano-twins were provided with the (111) twining interfaces, mainly for the 40 nm Ni/Ni_3Al-MoW multilayer. The reduction of the stacking fault energy (SFE) initiated by the co-doping of the Mo and W elements was deemed as promoting the formation of nano-twins. For the Ni/Ni_3Al-MoW multilayer with h = 10 nm, the nucleation and growth of the nano-twins were limited without observations due to the actual *h* being less than the critical thickness required for providing the stacking of the nano-twins;

(3) The hardness of the multilayer increased with a lower *h*, and the inhibitions of the dislocation movements due to both the grain refinements and layer interface barriers were responsible for the dominant strengthening mechanism. The elastic modulus of the multilayer decreased with $h \leq 40$ nm for the existence of the amorphous phase, and the superior resistance against the fracture was achieved with a higher H/E ratio due to toughening via the lamellar structure for the 10 nm Ni/Ni_3Al-MoW multilayer.

In conclusion, the Ni/Ni_3Al-MoW multilayer with h = 10 nm exhibited improved mechanical performances.

Author Contributions: C.Z.: Project administration, methodology, investigation, data analysis, funding acquisition, writing; L.S.: Data analysis; Y.D.: Writing—review & editing; D.L.: Literature search; Y.C.: Supervision. All authors have read and agreed to the published version of the manuscript.

Funding: This work was financially supported by the Natural Science Foundation of Jiangsu Province (BK20181027) and the Scientific Research Foundation of Nanjing Institute of Technology (YKJ201709).

Institutional Review Board Statement: Not applicable.

Informed Consent Statement: Not applicable.

Data Availability Statement: The data that support the findings of this study are available within this article.

Acknowledgments: The authors would like to thank the Natural Science Foundation of Jiangsu Province (BK20181027) and the Scientific Research Foundation of Nanjing Institute of Technology (YKJ201709) for funding this work, as well Shiyanjia Lab. (www.shiyanjia.com) for the XRD analysis.

Conflicts of Interest: The authors declare no conflict of interest.

References

1. Manvi, M.; Swamy, K.B.M. Microelectronic materials, microfabrication processes, micromechanical structural configuration based stiffness evaluation in MEMS: A review. *Microelectron. Eng.* **2022**, *263*, 111854. [CrossRef]
2. Choudhary, N.; Kaur, D. Shape memory alloy thin films and heterostructures for MEMS applications: A review. *Sens. Actuators A* **2016**, *242*, 162–181. [CrossRef]
3. Krogstad, J.A.; Keimel, C.; Hemker, K.J. Emerging materials for microelectromechanical systems at elevated temperatures. *J. Mater. Res.* **2014**, *29*, 1597–1608. [CrossRef]
4. Baumert, E.K.; Pierron, O.N. Fatigue degradation properties of LIGA Ni films using kilohertz microresonators. *J. Microelectromech. Syst.* **2012**, *22*, 16–25. [CrossRef]
5. Yuan, S.S.; He, G.; Zhang, M.; Li, G.Z. On the temperature-related mechanical properties of UV-LIGA nickel material. *Key Eng. Mater.* **2015**, *645*, 926–930. [CrossRef]
6. Yang, Y.; Imasogie, B.I.; Allameh, S.M.; Boyce, B.; Lian, K.; Lou, J.; Soboyejo, W.O. Mechanisms of fatigue in LIGA Ni MEMS thin films. *Mater. Sci. Eng. A* **2007**, *444*, 39–50. [CrossRef]
7. Cho, H.S.; Hemker, K.J.; Lian, K.; Goettert, J.; Dirras, G. Measured mechanical properties of LIGA Ni structures. *Sens. Actuators A* **2003**, *103*, 59–63. [CrossRef]
8. Zhang, M.; Pan, Y.; Zhou, Z.; Wei, L.I.; Hui, J.; Lei, W. Effect of heat treatment on tensile deformation behavior of Ni-Co film/Fe substrate systems. *Trans. Nonferr. Metal. Soc.* **2012**, *22*, 1613–1619. [CrossRef]
9. Talin, A.A.; Marquis, E.A.; Goods, S.H.; Kelly, J.J.; Miller, M.K. Thermal stability of Ni-Mn electrodeposits. *Acta Mater.* **2006**, *54*, 1935–1947. [CrossRef]
10. Laszczyńska, A.; Tylus, W.; Szczygieł, B.; Szczygieł, I. Influence of post-deposition heat treatment on the properties of electrodeposited Ni-Mo alloy coatings. *Appl. Surf. Sci.* **2018**, *462*, 432–443. [CrossRef]
11. Vamsi, M.V.N.; Wasekar, N.P.; Sundararajan, G. Influence of heat treatment on microstructure and mechanical properties of pulse electrodeposited Ni-W alloy coatings. *Surf. Coat. Technol.* **2017**, *319*, 403–414. [CrossRef]
12. Ong, C.Y.A.; Blackwood, D.J.; Li, Y. The effects of W content on solid-solution strengthening and the critical Hall-Petch grain size in Ni-W alloy. *Surf. Coat. Technol.* **2019**, *357*, 23–27. [CrossRef]
13. Costa, J.M.; Costa, J.G.R.; Neto, A.F.A. Techniques of nickel(II) removal from electroplating industry wastewater: Overview and trends. *J. Water Process. Eng.* **2022**, *46*, 102593. [CrossRef]
14. Esmaeili, A.R.; Mir, N.; Mohammadi, R. Influence of W content on microstructure and surface morphology of hard Ni-W films fabricated by magnetron co-sputtering. *J. Vac. Sci. Technol. A* **2021**, *39*, 033405. [CrossRef]
15. Borgia, C.; Scharowsky, T.; Furrer, A.; Solenthaler, C.; Spolenak, R. A combinatorial study on the influence of elemental composition and heat treatment on the phase composition, microstructure and mechanical properties of Ni-W alloy thin films. *Acta Mater.* **2011**, *59*, 386–399. [CrossRef]
16. Kurz, S.J.B.; Ensslen, C.; Welzel, U.; Leineweber, A.; Mittemeijer, E.J. The thermal stability of Ni-Mo and Ni-W thin films: Solute segregation and planar faults. *Scr. Mater.* **2013**, *69*, 65–68. [CrossRef]
17. Kurz, S.J.B.; Welzel, U.; Bischoff, E.; Mittemeijer, E.J. Diffraction stress analysis of highly planar-faulted, macroscopically elastically anisotropic thin films and application to tensilely loaded nanocrystalline Ni and Ni(W). *J. Appl. Crystallogr.* **2014**, *47*, 291–302. [CrossRef]
18. Armstrong, D.E.J.; Haseeb, A.S.M.A.; Roberts, S.G.; Wilkinson, A.J.; Bade, K. Nanoindentation and micro-mechanical fracture toughness of electrodeposited nanocrystalline Ni-W alloy films. *Thin Solid Film.* **2012**, *520*, 4369–4372. [CrossRef]
19. Yin, D.; Marvel, C.J.; Cui, F.Y.; Vinci, R.P.; Harmer, M.P. Microstructure and fracture toughness of electrodeposited Ni-21 at.%W alloy thick films. *Acta Mater.* **2018**, *143*, 272–280. [CrossRef]
20. Sim, S.D.; Krogstad, J.A.; Reddy, K.M.; Xie, K.Y.; Valentino, G.M.; Weihs, T.P.; Hemker, K.J. Nanotwinned metal MEMS films with unprecedented strength and stability. *Sci. Adv.* **2017**, *3*, e1700685. [CrossRef]
21. Sim, S.D.; Krogstad, J.A.; Xie, K.Y.; Dasgupta, S.; Valentino, G.M.; Weihs, T.P.; Hemker, K.J. Tailoring the mechanical properties of sputter deposited nanotwinned nickel-molybdenum-tungsten films. *Acta Mater.* **2018**, *144*, 216–225. [CrossRef]
22. Valentino, G.M.; Krogstad, J.A.; Weihs, T.P.; Hemker, K.J. Tailoring the coefficient of thermal expansion of ternary nickel alloys through compositional control and non-contact measurements. *J. Alloys Compd.* **2020**, *833*, 155024. [CrossRef]
23. Kim, K.; Park, S.; Kim, T.; Park, Y.; Sim, G.D.; Lee, D. Mechanical, electrical properties and microstructures of combinatorial Ni-Mo-W alloy films. *J. Alloys Compd.* **2022**, *919*, 165808. [CrossRef]
24. Navarro Yerga, R.M.; Pawelec, B.; Mota, N.; Huirache-Acuña, R. Hydrodesulfurization of Dibenzothiophene over Ni-Mo-W Sulfide Catalysts Supported on Sol-Gel Al_2O_3-CeO_2. *Materials* **2022**, *15*, 6780. [CrossRef]
25. Singh, R.; Kunzru, D.; Sivakumar, S. Enhanced catalytic activity of ultrasmall NiMoW trimetallic nanocatalyst for hydrodesulfurization of fuels. *Fuel* **2021**, *288*, 119603. [CrossRef]
26. Tavizón-Pozos, J.A.; Suárez-Torello, V.A.; de los Reyes, J.A.; Guevara-Lara, A.; Pawelec, B.; Fierro, J.L.G.; Vrinat, M.; Geantet, C. Deep hydrodesulfurization of dibenzothiophene over NiW sulfide catalysts supported on sol-gel titania-alumina. *Top. Catal.* **2016**, *59*, 241–251. [CrossRef]

27. Allam, M.; Benaicha, M.; Dakhouche, A. Electrodeposition and characterization of NiMoW alloy as electrode material for hydrogen evolution in alkaline water electrolysis. *Int. J. Hydrogen Energy* **2018**, *43*, 3394–3405. [CrossRef]
28. Li, H.; Xie, M.; Zhang, G.; Fan, X.; Li, X.; Zhu, M.; Wang, L. Structure and tribological behavior of Pb-Ti/MoS_2 nanoscaled multilayer films deposited by magnetron sputtering method. *Appl. Surf. Sci.* **2018**, *435*, 48–54. [CrossRef]
29. Shang, K.; Zheng, S.; Ren, S.; Pu, J.; He, D.; Liu, S. Improving the tribological and corrosive properties of MoS_2-based coatings by dual-doping and multilayer construction. *Appl. Surf. Sci.* **2018**, *437*, 233–244. [CrossRef]
30. Liu, Z.R.; Xu, Y.X.; Peng, B.; Wei, W.; Chen, L.; Wang, Q. Structure and property optimization of Ni-containing AlCrSiN coatings by nano-multilayer construction. *J. Alloys Compd.* **2019**, *808*, 151630. [CrossRef]
31. Zhou, C.; Wang, J.; Meng, J.; Li, W.; Liu, P.; Zhang, K.; Ma, F.; Ma, X.; Feng, R.; Liaw, P.K. Effects of modulation layer thickness on fracture toughness of a TiN/AlN-Ni multilayer film. *Mater. Des.* **2022**, *222*, 111097. [CrossRef]
32. Mei, F.; Zhang, Z.; Yu, Y.; Lin, X.; Gao, J.; Yuan, T.; Lin, J. Microstructure, mechanical, tribological, and oxidizing properties of AlCrSiN/AlCrVN/AlCrNbN multilayer coatings with different modulated thicknesses. *Ceram. Int.* **2022**, *48*, 32973–32985. [CrossRef]
33. Liu, D.; Zhang, P.; Meng, L.; Ruan, C.; Liang, Y.; Tu, J. Structure, mechanical properties and tribological behavior of sp2-C:Ti/sp3-C:Ti multilayer films deposited by magnetron sputtering. *Diam. Relat. Mater.* **2022**, *125*, 108963. [CrossRef]
34. Zhang, C.; Feng, K.; Li, Z.; Lu, F.; Huang, J.; Wu, Y.; Chu, P.K. Enhancement of high-temperature strength of Ni-based films by addition of nano-multilayers and incorporation of W. *Acta Mater.* **2017**, *133*, 55–67. [CrossRef]
35. Zhang, C.; Zhang, B.; Xie, L. Improving mechanical properties of Ni-W based nanocrystalline films by multilayered architecture. *Surf. Coat. Technol.* **2020**, *402*, 126341. [CrossRef]
36. Zhou, H.; Chang, L.; Fu, K.; Huang, H.; Niu, R.; Liao, X.; Sheppard, L.; George, L.; Martinu, L. Improvement of flow strength and scratch resistance of Ti/Cu nanocrystalline metal multilayer thin films by tailoring layer thickness and modulation ratio. *Surf. Coat. Technol.* **2020**, *404*, 126461. [CrossRef]
37. Xue, J.; Li, Y.; Gao, L.; Qian, D.; Song, Z.; Wang, X.; Zhu, X.; Chen, J. Effects of periods on the evolution of microstructure and mechanical properties of multilayered Cu-W films during thermal annealing. *Surf. Coat. Technol.* **2020**, *381*, 125179. [CrossRef]
38. Holzwarth, U.; Gibson, N. The Scherrer equation versus the 'Debye-Scherrer equation'. *Nat. Nanotechnol.* **2011**, *6*, 534. [CrossRef]
39. Oliver, W.C.; Pharr, G.M. An improved technique for determining hardness and elastic modulus using load and displacement sensing indentation experiments. *J. Mater. Res.* **1992**, *7*, 1564–1583. [CrossRef]
40. Zhang, H.S.; Endrino, J.L.; Anders, A. Comparative surface and nano-tribological characteristics of nanocomposite diamond-like carbon thin films doped by silver. *Appl. Surf. Sci.* **2008**, *255*, 2551–2556. [CrossRef]
41. Wei, M.Z.; Huo, J.Z.; Wang, C.C.; Ma, Y.J.; Pan, H.Z.; Cao, Z.H.; Meng, X.K. Tuning length scale effect of hardness in Ag/Nb/Cu/Nb multilayers by Nb amorphous interlayer. *Mater. Sci. Eng. A* **2022**, *835*, 142651. [CrossRef]
42. Messier, R.; Giri, A.P.; Roy, R.A. Revised structure zone model for thin film physical structure. *J. Vac. Sci. Technol. A* **1984**, *2*, 500–503. [CrossRef]
43. Zong, J.; Feng, K.; Li, Z.; Qasim, A.M.; Chu, P.K. Studies on the surface morphology and hydrophobic property of NiTi thin films under in situ and post annealing various temperatures. *Mater. Lett.* **2016**, *183*, 244–247. [CrossRef]
44. Tang, M.; Du, Y.; Zhou, P.; Wang, S.; Zhang, H.; Zeng, Y.; Liu, S.; Chai, X.; Peng, Y.; Wu, C.; et al. Experimental phase diagram, thermodynamic modeling and solidified microstructure in the Mo–Ni–W ternary system. *Calphad* **2020**, *68*, 101748. [CrossRef]
45. Valentino, G.M.; Shetty, P.P.; Chauhan, A.; Krogstad, J.A.; Weihs, T.P.; Hemker, K.J. Nanotwin formation in Ni–Mo–W alloys deposited by dc magnetron sputtering. *Scr. Mater.* **2020**, *186*, 247–252. [CrossRef]
46. Zhu, Y.T.; Liao, X.Z.; Wu, X.L. Deformation twinning in nanocrystalline materials. *Prog. Mater. Sci.* **2012**, *57*, 1–62. [CrossRef]
47. Li, B.Q.; Sui, M.L.; Mao, S.X. Twinnability predication for fcc Metals. *J. Mater. Sci. Technol.* **2011**, *27*, 97–100. [CrossRef]
48. Chen, Y.; Yu, K.Y.; Wang, H.; Chen, J.; Zhang, X. Stacking fault and partial dislocation dominated strengthening mechanisms in highly textured Cu/Co multilayers. *Int. J. Plast.* **2013**, *49*, 152–163.
49. Zhang, Z.; Shao, C.; Wang, S.; Luo, X.; Zheng, K.; Urbassek, H.M. Interaction of Dislocations and Interfaces in Crystalline Heterostructures: A Review of Atomistic Studies. *Crystals* **2019**, *9*, 584. [CrossRef]
50. Callisti, M.; Polcar, T. Combined size and texture-dependent deformation and strengthening mechanisms in Zr/Nb nano-multilayers. *Acta Mater.* **2017**, *124*, 247–260. [CrossRef]
51. Zhang, J.Y.; Zhang, X.; Wang, R.H.; Lei, S.Y.; Zhang, P.; Niu, J.J.; Liu, G.; Zhang, G.J.; Sun, J. Length-scale-dependent deformation and fracture behavior of Cu/X (X = Nb, Zr) multilayers: The constraining effects of the ductile phase on the brittle phase. *Acta Mater.* **2011**, *59*, 7368–7379. [CrossRef]
52. Rupert, T.J.; Trenkle, J.C.; Schuh, C.A. Enhanced solid solution effects on the strength of nanocrystalline alloys. *Acta Mater.* **2011**, *59*, 1619–1631. [CrossRef]
53. Zhang, C.; Feng, K.; Li, Z.; Lu, F.; Huang, J.; Wu, Y.; Chu, P.K. Enhancement of hardness and thermal stability of W-doped Ni_3Al thin films at elevated temperature. *Mater. Des.* **2016**, *111*, 575–583. [CrossRef]
54. Misra, A.; Hirth, J.P.; Hoagland, R.G. Length-scale-dependent deformation mechanisms in incoherent metallic multilayered composites. *Acta Mater.* **2005**, *53*, 4817–4824. [CrossRef]
55. Anderson, P.M.; Foecke, T.; Hazzledine, P.M. Dislocation-based deformation mechanisms in metallic nanolaminates. *MRS Bull.* **1999**, *24*, 27–33. [CrossRef]

56. Zhou, Q.; Xie, J.Y.; Wang, F.; Huang, P.; Xu, K.W.; Lu, T.J. The mechanical behavior of nanoscale metallic multilayers: A survey. *Acta Mech. Sin.* **2015**, *31*, 319–337. [CrossRef]
57. Li, Y.; Ma, J.; Liaw, P.K.; Zhang, Y. Exploring the amorphous phase formation and properties of W-Ta-(Cr, Fe, Ni) high-entropy alloy gradient films via a high-throughput technique. *J. Alloys Compd.* **2022**, *913*, 165294. [CrossRef]
58. Li, R.N.; Song, H.Y.; An, M.R.; Xiao, M.X. Atomic-scale insight into mechanical properties and deformation behavior of crystalline/amorphous dual-phase high entropy alloys. *Phys. Lett. A* **2022**, *446*, 128272. [CrossRef]
59. Leyland, A.; Matthews, A. On the significance of the H/E ratio in wear control: A nanocomposite coating approach to optimised tribological behaviour. *Wear* **2000**, *246*, 1–11. [CrossRef]
60. Matthews, A.; Jones, R.; Dowey, S. Modelling the Deformation Behaviour of Multilayer Coatings. *Tribol. Lett.* **2001**, *11*, 103–106. [CrossRef]